Combined MRI and Optical Computed Tomography: Literature Review

Ciara McErlean

23/1/13

1 Introduction

Multiparametric imaging is very important in cancer imaging. It allows the cross-correlation of observations at tumour level and allows validation of new biomarkers against an established standard [1]. This is the goal for combined MRI and OptCT imaging of tumours.

2 Theory

2.1 Radon Space

When light passes through a substance, it is assumed to be attenuated by some small amount of intensity ΔI over a small distance Δy

$$\frac{\Delta I}{I} = -\mu(y)\Delta y \tag{1}$$

where $\mu(y)$ is the linear attenuation coefficient. Taking the infinitesimal limit and integrating,

$$\int_{I_0}^{I} \frac{1}{I}\,\mathrm{d}I = -\int_{L} \mu(y)\,\mathrm{d}y \tag{2}$$

this leads to Beer's Law

$$I(y) = I_o(y)\mathrm{e}^{-\int_L \mu(y)\,\mathrm{d}y} \tag{3}$$

where I_0 is the intensity with no attenuation and $I(y)$ is the intensity at depth y. L is the path the light ray has followed. The integral in the exponential term of Beer's Law takes into account the differences in attenuation coefficient along the path L.

From equation 3 it is apparent that the intensity of a light beam after passing through a sample gives information about the line integral of the function μ along the line L. The CT scanning process records this information for many lines L at different lateral positions and it is from this information that we reconstruct a map of μ [2]. The Radon transform maps a function into a set of its line integrals. Therefore, CT reconstruction involves an inverse Radon transform.

To build a 2-D map of attenuation coefficients, line integrals must be measured from multiple angles (see Figure 1). If the sample rotates by some angle ϕ then the attenuation seen at position (x, y) changes. The Radon transform, often called a projection or a view, is defined as

$$P_\phi(x) = \int\limits_{sample} \mu(x', y')\,\mathrm{d}y = -\ln\left(\frac{I_\phi(x)}{I_0}\right) \tag{4}$$

where

$$
\begin{aligned}
x' &= x\cos\phi + y\sin\phi \\
y' &= -x\sin\phi + y\cos\phi
\end{aligned}
\tag{5}
$$

The projection information is stored in what is known as 'Radon space' with dimensions (x, ϕ). Radon space is filled by measuring the projection value for all combinations of x and ϕ. A filled Radon space diagram is often referred to as a sinogram (see Figure 2).

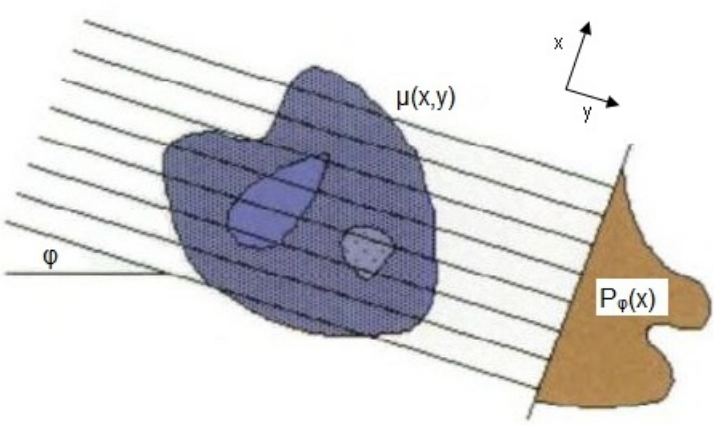

Figure 1: Parallel ray geometry showing how a projection/view, $P_\phi(x)$, is recorded at angle ϕ. The attenuation $\mu(x, y)$ within the sample is not uniform and projections must be taken from many angles to reconstruct a map of $\mu(x, y)$. Here x represents lateral position and y represents depth. Figure adapted from [3].

In practice, the finite number of lines L limits the resolution of reconstructions. There are two geometries for 2-D reconstructions; parallel beam and fan beam. The choice of scanning geometry also affects the resolution [2].

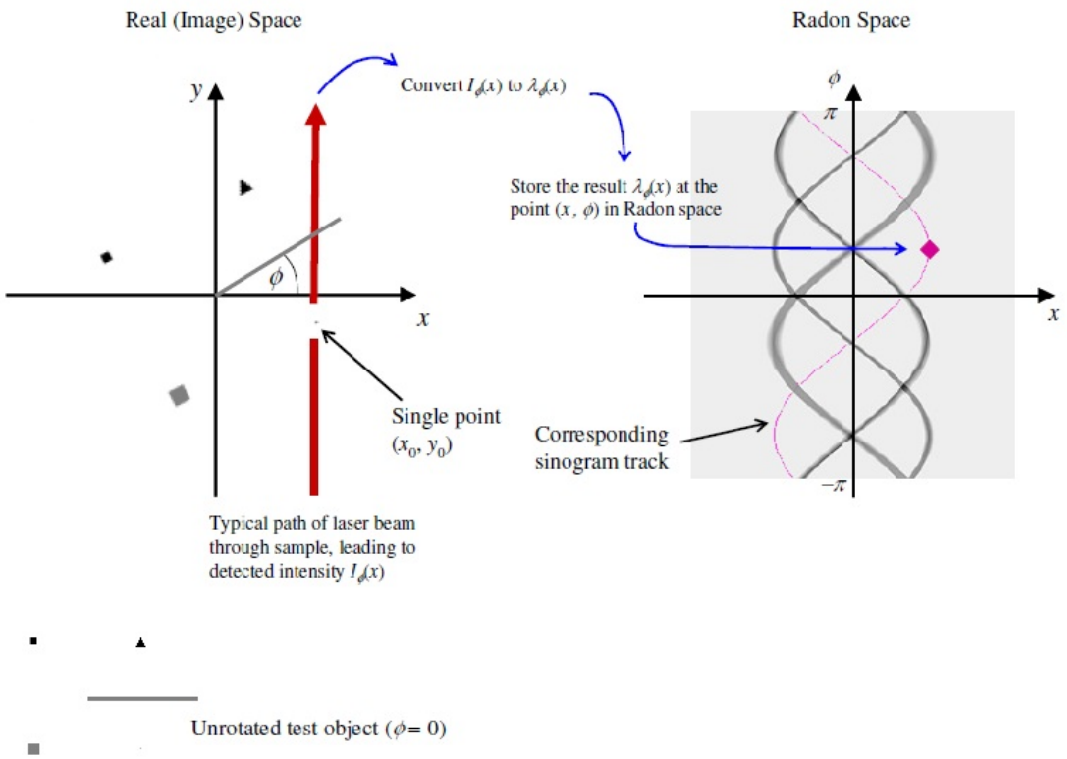

Figure 2: Transformation from image space to Radon space demonstrated. Projection information is stored in Radon space. A 2-D image of Radon space is often called a sinogram. Different shapes produce characteristic tracks on the sinogram according to their symmetry upon rotation. Figure adapted from [4].

2.2 Filtered Back-projection

The information stored in a sinogram is used to reconstruct a map of attenuation within the sample. This is done through the process of back-projection.

Simple back-projection involves taking each projection point $P_\phi(x)$ and working back along the line integral, L, which created that projection in real space. Each point along L is attributed with the value $P_\phi(x)$. After doing this for all projection points, certain areas in real space are shaded darker as projections from different angles cross over. This builds up a picture of the shapes inside the sample.

Mathematically, back-projection can be described in terms of Fourier transforms (FTs). The 1-D FT of projection data for angle, ϕ, is given by

$$S_\phi(k_x) = \int P_\phi(x) \mathrm{e}^{-ixk_x} \, \mathrm{d}x \tag{6}$$

where the FT maps $P_\phi(x)$ from the spatial domain to $S_\phi(k_x)$ in the frequency domain, also known as k-space.

For the case of $\phi = 0$ this can be written as

$$S_0(k_x) = \iint \mu(x, y) \mathrm{e}^{-ixk_x} \, \mathrm{d}x\mathrm{d}y \tag{7}$$

$$= \iint \mu(x, y) \mathrm{e}^{-i(k_x x + k_y y)} \, \mathrm{d}x\mathrm{d}y \tag{8}$$

$$= \tilde{\mu}(k_x, k_y = 0) \tag{9}$$

where $\tilde{\mu}(k_x, k_y)$ is the 2-D FT of $\mu(x, y)$. The extra term in (8) is added under the assumption that $k_y = 0$ giving $\mathrm{e}^{k_y y} = \mathrm{e}^0 = 1$.

Since the co-ordinate system can be chosen arbitrarily, equations (7-9) can be generalised for any angle ϕ. This is formalised in the Fourier Slice Theorem which states that the 2-D FT of $\mu(x, y)$ along the line at ϕ in k space is the same as the 1-D FT of the projection, $P_\phi(x)$ [4].

However, simple back-projection is flawed. As all the projections cross in the middle of the image, an artefact of high attenuation builds up there and edges of features in the sample are blurred. In order to reconstruct more accurate images a mathematical trick called Filtered Back-projection (FBP) is used.

The blurring is similar to that of an out-of-focus system with point spread function (PSF) proportional to $1/f$ where f is the frequency [3]. Therefore, to remove this blurring effect the image should be multiplied by the inverse of the blurring function in frequency space.

Therefore, the formula for reconstructing $\mu(x, y)$ using FBP involves a 2-D inverse FT of $S_\phi(k)$

$$\mu(x,y) = \frac{1}{2\pi}\iint \tilde{\mu}(k_x,k_y)\mathrm{e}^{i(k_x x+k_y y)}\,\mathrm{d}k_x\mathrm{d}k_y \tag{10}$$

Converting to polar coordinates where $k_x = k\cos\phi$ and $k_y = k\sin\phi$ gives

$$\mu(x,y) = \frac{1}{2\pi}\int_0^{2\pi}\int_0^{\infty} \tilde{\mu}(k,\phi)\mathrm{e}^{ik(x\cos\phi+y\sin\phi)}k\,\mathrm{d}k\mathrm{d}\phi \tag{11}$$

$$= \frac{1}{2\pi}\int_0^{2\pi}\left[\int_0^{\infty} S_\phi(k)\mathrm{e}^{ikx'}k\,\mathrm{d}k\right]\,\mathrm{d}\phi \tag{12}$$

$$= \frac{1}{2\pi}\int_0^{2\pi} Q_\phi(x')\,\mathrm{d}\phi \tag{13}$$

where $Q_\phi(x')$ is the projection filtered by in the frequency domain by multiplication with k. This is known as the ideal inverse filter, giving high weighting to high frequency components but low weighting to low frequencies. Other commonly used filters include the Hann, Hamming, Butterworth, Shepp-Logan and Ram-Lak. Choice of filter can affect the quality of reconstructions [3].

In order to use the FBP to reconstruct projections from OptCT two requirements of the Fourier Slice theorem must be satisfied. The first is that projections should be the result of rays travelling parallel to the optical axis through the sample. The second is that all points along a projection should contribute with the same weighting to the signal [5]. OptCT design considerations focus on satisfying these requirements to obtain high quality images.

2.3 Optics

(See Walls 2007) Resolution for an optical system is given by the Rayleigh criterion,

$$r_{Airy} = \frac{0.61n\lambda}{\mathrm{NA}} \tag{14}$$

where r_{Airy} is the radius of the Airy function which is a measure of resolution in the focal plane. n is the refractive index of the medium around the lens, λ is the wavelength of light and NA is the numerical aperture of the lens.

Depth of field (DOF) is given by [REF]

$$DOF = n_{bath}(\frac{n\lambda}{\mathrm{NA}^2} + \frac{n}{M\mathrm{NA}}e) \tag{15}$$

where e is the pixel size of the CCD, n_{bath} is the refractive index of the medium surrounding the specimen and M is the lateral magnification.

According to Nyquist the Airy disc must be sampled more than twice per DOF distance to avoid aliasing. This constrains the detector spacing to

$$e \leq M\frac{r_{Airy}}{2} \tag{16}$$

so the maximum possible DOF is given by

$$DOF_{max} = n_{bath}(\frac{1.305\lambda}{\mathrm{NA}^2}) \tag{17}$$

Shows trade-off between high resolution with high NA and high DOF with low NA. Generally choose NA based on size of sample. [Say how this impacts on scanning process, include sinogram from Doran 2010 PMB. Refer to discussion of Sharpe's set-up and DOF]

2.4 Common artefacts

Axis of rotation problems. Corrections suggested by many groups. Recently by Dong in 2012 [6] discuss method.

Walls 2005 *Noise is Poisson distributed below 2% on an averaged signal. Therefore artefactual effects must be kept below 1%*

3 Dosimetry

3.1 Laser scanning configuration

One of the first reported optical computed tomography (OptCT) systems was developed in the area of gel dosimetry. Accurate 3-D measurement of dose delivery in radiotherapy is extremely important in developing safe treatment plans. Specialist polymer gels, such as BANG® [7], respond to irradiation with changes in optical attenuation and scattering properties. This makes them ideal for measuring 3-D dose distributions. Previously the irradiated gels were measured by MRI and x-ray CT. However, these are expensive imaging modalities. In 1996, Gore and Maryanski published the first system for scanning polymer gels using optical computed tomography [8]. In later comparisons, OptCT has been found to be more precise, have reduced noise and smoother line profiles than MRI for gel dosimetry [9]. [DISPUTED PAPER]

Gore's system consisted of a He-Ne laser source and large area photo-diode detector (see Figure 3). Translate-rotate acquisition was employed whereby the sample was rotated and projection data acquired by the photo-diode over 360°. Small angular steps between projections are necessary for high quality reconstruction [3]. For a 2-D reconstruction, projections are acquired for multiple spots across a slice of the sample by translating the laser beam using mirrors. For 3-D information, the sample height had to be manually adjusted and many 2-D slices acquired. This meant scanning an entire sample took hours and lengthy scanning times are the chief disadvantage of the laser scanning method. Accuracy of 5% is reported and spatial resolution of 2mm, which is roughly the same as the laser beam width [8].

The idea of OptCT scanning in dosimetry was quickly developed by other groups. Laser scanning set-ups were published in 1996 by Tarte *et al.*, [10] and Kelly *et al.* [REF] *Can't find the paper 1996 Kelly references in 1998 [11] Med Phys says it doesn't exist.* Kelly *et al.* claim to have independently developed their scanner which is very similar to that of Gore's. In in both Kelly's and Tarte's scanners, the sample is rotated and translated using a stage whereas Gore used mirrors to translate the laser spot across the sample.

A commercial laser scanning OptCT system, OCTOPUS^{TM}by MGS Research, Inc. (Madison, CT), is an extension of Gore's original set-up with the addition of a platform capable of vertical movement for automated slice-selection [12]. For a number

of years it was the only commercially available system and has been characterised by several groups [12–15]. According to Oldham, characterisation of OptCT systems should include checks on geometric distortion, accuracy of reconstruction, scatter artefacts and reflection and refraction artefacts [16].

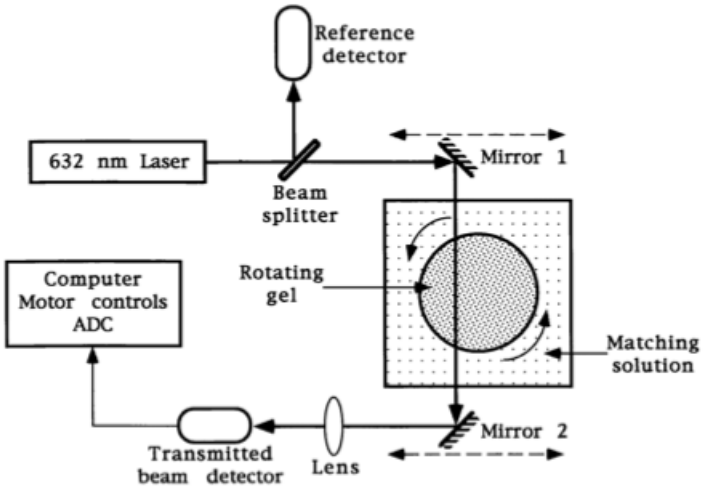

Figure 3: A first generation, Laser Scanning OptCT system developed by Gore. The sample is rotated and projections recorded at a number of angles. The mirrors scan the laser beam across the sample but movement in the vertical direction is by manual adjustment only Figure adapted from [8].

Laser scanning systems include a beam splitter before the sample to create a reference beam. Dividing projections by the reference intensity corrects for laser beam intensity fluctuations [8].

Refraction and reflection at container walls are significant concerns for all configurations of dosimetry with OptCT. Generally, laser beams are incident on the gel container at a small angle, such as 5°, to avoid large reflection at the interface. In addition, the gel container is usually placed in a tank containing 'matching fluid' with a refractive index close to that of the gel. This prevents significant refraction as the light passes into the gel. Doran found through ray tracing simulations that the refractive index of the walls of the matching tank and gel container are not important compared to the gel and matching fluid. The optimum difference in refractive index between these two was interestingly found to be non-zero [17].

To maximise the dynamic range of the system, coloured dye is commonly added to the matching fluid so both the refractive index and optical density of the matching fluid and gel are very similar [18].

3.2 Pixelated detector based systems

[**MENTION WINFREE**] In 1997 the first charge coupled device (CCD) camera based OptCT system was published by Tarte *et al.* which employed an incoherent white light source and CCD camera detection [19]. The advantage of a pixelated detector based system is that an entire 2-D projection can be imaged at once, potentially increasing the scanning speed by several orders of magnitude depending on the data through-put rate. Tarte's system used a divergent light source and diffusing screen to measure optical density in a thin gel section (see Figure 4).

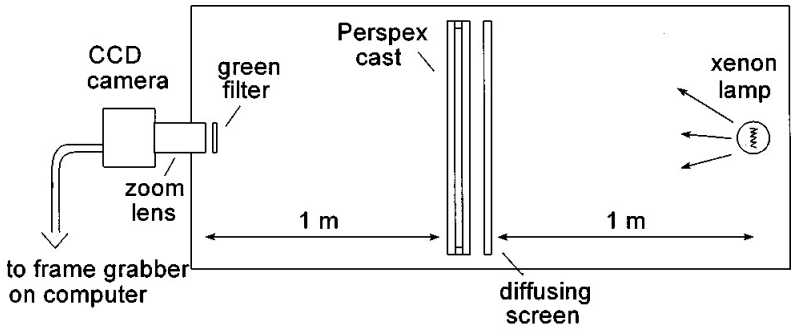

Figure 4: Diagram of the first CCD-based OptCT system, developed by Tarte *et al.* It uses divergent illumination from a white light source and CCD camera detection to record an entire 2D projection at once. Figure adapted from [19].

The accuracy of Tarte's system was checked by comparison with the standard measure of dosimetry, the parallel plate ionisation chamber. It was found to be on average within 3% of the value from the ionisation chamber [19]. A comparison between Tarte's laser scanning and CCD set-ups found that they had similar spatial resolutions. The CCD method had improved speed of acquistion but suffered from consistently worse SNR as a photodiode detector can collect many more photons per 'pixel' than a CCD camera [19].

Advances in technology have meant that high quality detectors are much more af-

fordable. A cheaper alternative to very high quality CCD cameras is the CMOS (Complementary Metal-Oxide-Semiconductor) detector which has the potential for higher resolution and dynamic range [4]. Using a higher quality detector would improve many OptCT systems in terms of scanning speed and reduced artefacts [17,19].

Parallel beam configuration: One method to reconstruct 3-D images with a CCD or CMOS detector is to create a broad parallel beam. This allows the use of parallel reconstruction algorithms, very similar to those used for x-ray CT. Each 2-D projection image recorded corresponds to one row for every slice in the 3-D reconstruction sinogram [4]. Telecentric optics, in which the chief rays are parallel to the optical axis, are key in the design of this configuration [20]. Telecentric optics can be achieved either through a careful arrangement of a large converging lens before the sample and standard camera lens [17] (see Figure 5) or through an expensive telecentric lens [21]. The process of forming a parallel beam results in non-uniformities in the lightfield. This is compensated for by dividing by a 'correction' or 'open lightfield', image which is a projection taken with no sample in the tank [17].

Telecentric lenses give the advantages of parallel rays and almost constant magnification throughout the sample [22]. This helps to satisfy the requirements of the Fourier Slice Theorem for high quality reconstruction mentioned in Section 2.2.

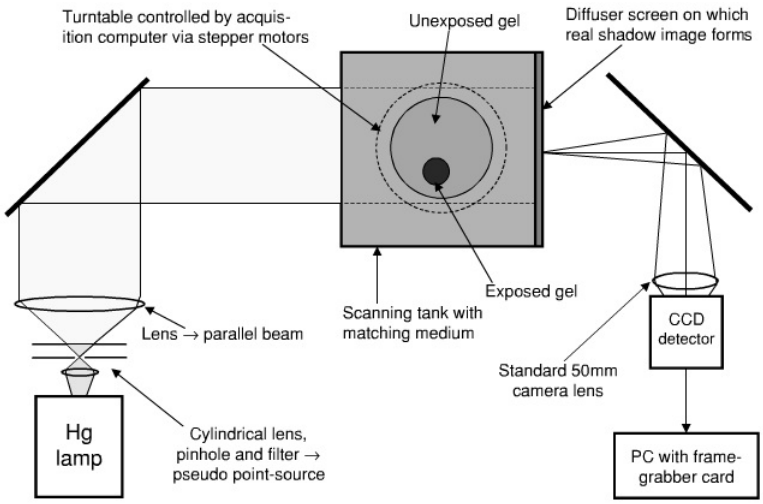

Figure 5: Diagram of a parallel beam OptCT system, developed by Doran *et al.* Telecentric optics create a parallel beam. Figure adapted from [17].

Initial systems suffered from 'graininess' due to the unstable gain of cheap CCD cameras and granularity of the diffusing screen [17]. Superior optics meant later systems did not require a diffuser and instead lenses were used to image directly onto the CCD. More recent CCD and CMOS camera designs have also vastly improved OptCT system quality

Cone beam configuration: Wolodzko *et al.* published the first cone beam OptCT system with CCD detection for gel dosimetry [24]. One advantage of this configuration is the optics for producing a cone beam are much simpler than those for producing accurate parallel beams [4]. However, the reconstruction is computationally more complex [25]. A commercial cone-beam system, Vista^{TM}by Modus Medical Devices Inc. (London, ON, Canada), is available and reviewed recently by Olding *et al.* [26].

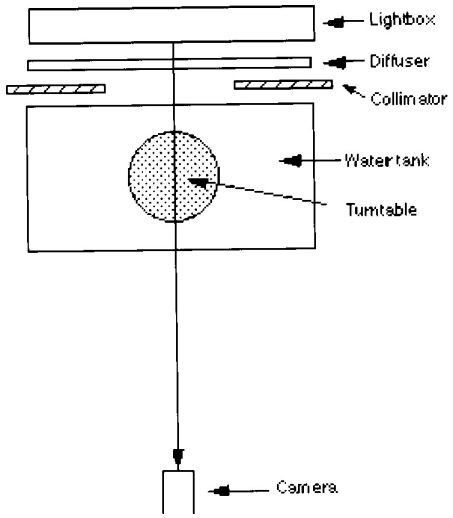

Figure 6: Cone-beam CCD configuration (figure from [24]).

There has not been experimental comparison of parallel and cone-beam systems. However, Doran suggests that while cone-beam is usually somewhat cheaper due to simplified optics, modern parallel-beam systems have better scatter-rejection and may have fewer stray light problems [4, 26, 27].

4 Tissue imaging

4.1 Optical Projection Tomography

Another version of OptCT was developed by Sharpe *et al.* in the area of 3-D microscopy for gene expression studies [28]. Although this set-up in 2002 came after Gore's they are apparently independent and Sharpe named his technique Optical Projection Tomography (OPT).

Other techniques for 3-D microscopy are well established however, OPT offers some unique advantages. Confocal microscopy is offers high resolution images up to a depth of about 1mm [29]. However, it is limited to fluorescent signals meaning many optical stains used routinely in histology would not work. Optical coherence tomography (OCT), which is commonly used in ophthalmology, is capable of micrometer-scale resolution with depth limited to 2-3mm in tissue [30]. Both of these techniques generate tomographic images through sectioning whereas OPT is a projection based tomography technique [31]. Avoiding sectioning is important in producing truly representative 3-D images [22]. Another advantage of OPT is its ability to image much larger specimen, with depth of around 3cm being reported [22]. This superior imaging depth not just due to clarification of the samples, discussed in Section 5. OCT and confocal systems have also been tested with clearing agents and the reported gains in depth vary between 20-150% in OCT [32] which is significantly shallower than OptCT.

Sharpe's original system uses a microscope to focus projections of a mouse embryo onto a camera imaging chip. Image-focusing optics are one difference between OPT and x-ray CT, which records shadows of the sample [28]. Sharpe reports some impressive images as reproduced in Figure 7. Use of the microscope gives resolution of about 5-10μm meaning single-cell membranes, around 10μm thick, can be seen [28]. However, the high NA optics which give high resolution limit the depth of field (DOF). Sharpe decided to circumvent the problem of a low DOF by positioning the rotational axis so only half the specimen was in focus at once and the specimen was scanned 360° to collect in-focus data from all points. The problem with only having half of specimen in focus at once is that unfocused light is superimposed upon the focused data and included in the reconstruction. This leads to blurring which is worse with distance from the axis of rotation. Walls proposed a method of correcting this defocusing effect using a frequency-distance filter, as described by Xia for SPECT [33, 34]. The filter narrows the PSF to in-focus data allowing in-focus,

high resolution images to be reconstructed [34].

In dosimetry the refractive index within the polymer gels was roughly uniform. In tissue this is not the case, with scattering and refraction occurring at cell membrane interfaces. To make high resolution reconstruction through back projection possible, light paths through the specimen must be able to be approximated as parallel line integrals, meaning refraction must be minimised. A process called optical clearing or clarification is employed which renders tissue optically transparent. An optical clearing agent (OCA) replaces the lower refractive index intra-cellular fluid acting as a matching fluid within the sample itself. The mechanism for this differs between agents, see Section 5 for more detail.

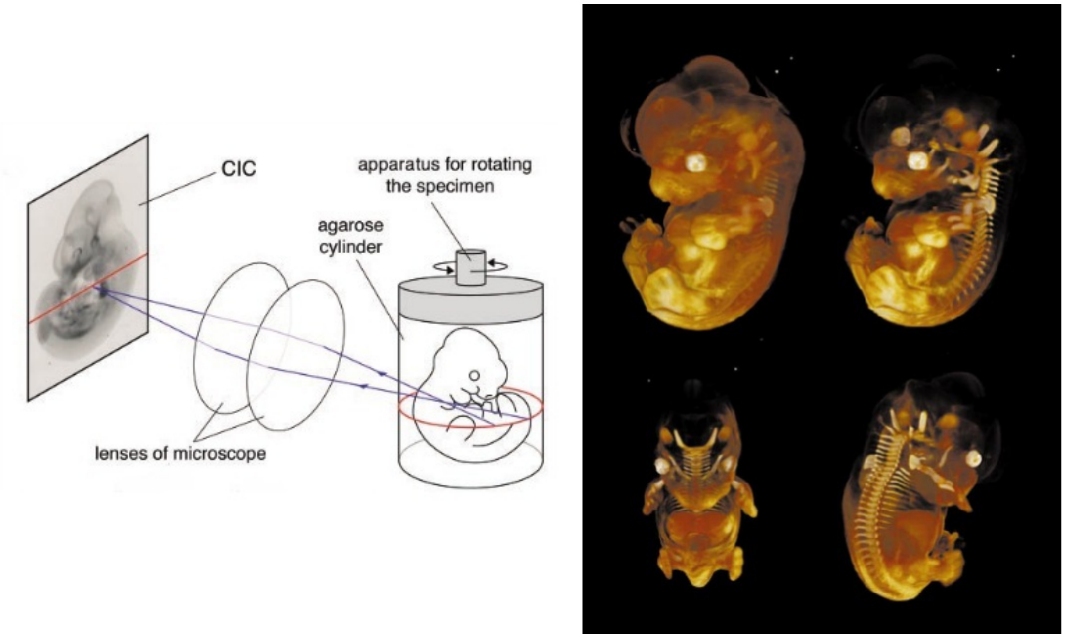

(a) OPT setup (b) Mouse images

Figure 7: Part (a) shows the optical set-up for the first OPT system by Sharpe. CIC indicates the camera imaging chip. A microscope is used to focus projection images onto the CIC. The specimen is set in agarose gel for stability. Figure adapted from [28]. Part (b) shows some false colour images of a TS21 mouse embryo stained with alcian blue and imaged with OPT. The images have varying degrees of opacity allowing control of which internal organs are seen. Figure adapted from [31].

In 2005 Fauver reported a modified version of OPT capable of imaging single cell nuclei with 0.9μm resolution (see Figure 8) [35]. The OPT microscope includes a rotation stage and piezoelectrically driven objective lens. In a technique similar to Hausler [36] the objective lens is scanned axially to create an extended DOF image which is also known as a pseudo-projection. The extended DOF means features have the same focus from all angles, allowing high resolution reconstruction. However, this is not a truly quantitative technique, hence pseudo and not true projections are recorded. A high numerical aperture (NA) lens gives high resolution at the expense of low depth of field. If such high resolution is not required, low NA optics such as those used by Sharpe would be a more quantitative way to generate projections than scanning a high NA lens.

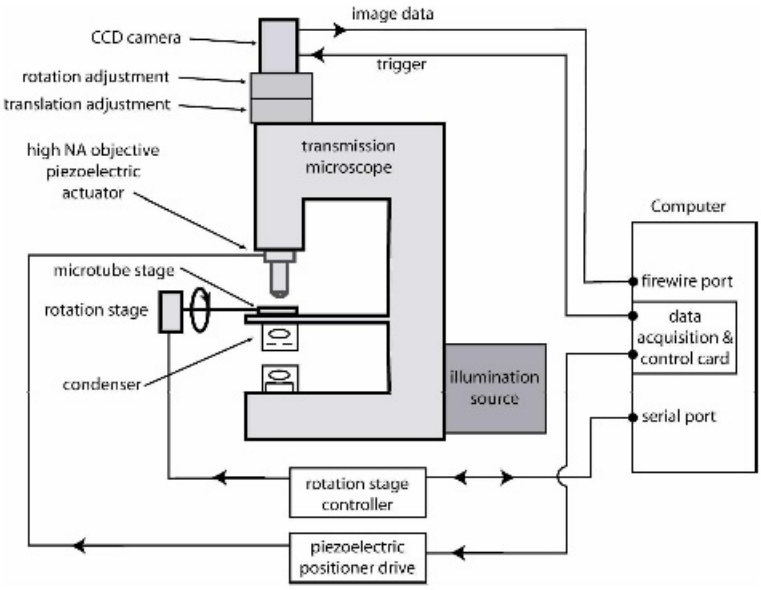

Figure 8: OPT microscope for imaging single cell nuclei. A microcapillary tube injected with cells is rotated with sub-micron precision and refractive index matching to 0.02. The piezoelectric objective lens is scanned axially to create extended depth of field images. Figure adapted from [35].

Wang and Wang report an improvement to OPT giving higher axial and lateral resolution, even for slices far from the optical axis [5, 37]. As previously mentioned, to obtain high quality reconstructions the projections should closely approximate a line integral of parallel rays passing through the sample [37]. This is not exactly the case for OPT, limiting the best resolution possible. Wang proposed placing an iris at

the back focus of the objective lens. This reduces divergence of the projection rays from paths parallel to the optical axis giving qualitatively better resolution.

4.2 Fluorescent/emission OptCT

Sharpe was the first to identify the possibility of using OPT to image fluorescent stains in biological specimen [28]. There are a wide range of fluorescent optical stains in use in histology making this development particularly useful for biological imaging. It also offers the advantage of being able to record multiple signals independently unlike transmission OPT (tOPT) [28].

Optical emission CT (OptECT) also known as emission OPT (eOPT) is the optical equivalent of SPECT (single photon emission computed tomography) [22]. Instead of measuring the attenuation of photons through a sample (tOPT), eOPT signal comprises of fluorescence photons emitted along a ray path [20].

Some changes from the set-up (see Figure 9) from tOPT include the addition of a narrow bandwidth excitation filter before the sample. This selects for the excitation wavelength of the fluorescent marker being used in the sample. The illumination is perpendicular to the detector to avoid detection of the illumination light rather than fluorescence. An emission filter before detector selects for the longer emission wavelength of the fluorophores, again to avoid contamination from auto-fluorescent and ambient photons being picked up by the CCD. To avoid photobleaching systems often include a shutter to turn off the lamp when not imaging. The image forming optics is the same as for tOPT, although the reconstruction and artefacts are different [20].

Oldham *et al.* have made several improvements on Sharpe's eOPT set-up by changing from microscope to bench-top apparatus [22,38]. Microscope based systems suffer from poor DOF as the optics are designed to image flat samples. Oldham's custom made set-up, which is closer to the dosimetry systems previously seen, employs telecentric optics giving much improved DOF capable of imaging samples up to 3cm [22]. However, better DOF is achieved at the cost of worse lateral spatial resolution and this trade-off must be considered with respect to the information required from the specimen [18].

[Was Oldham really trying to improve OPT or just adapting OptCT dosimetry system? Is there detailed comparison? If not then could be an

aspect of PhD]

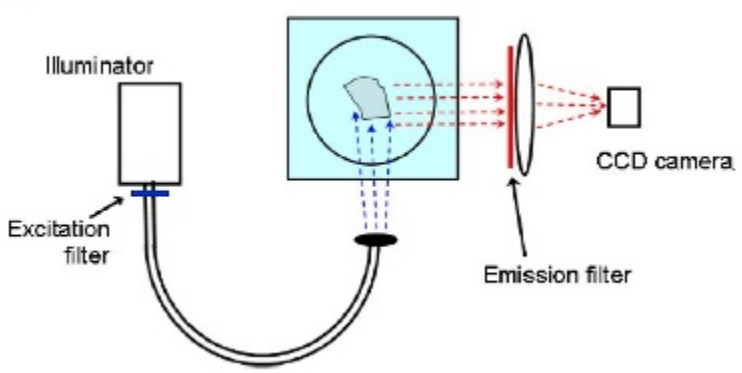

Figure 9: Example of setup for OptECT/eOPT imaging. Filters are used to select for the excitation and emission wavelengths of the fluorescent stain. This set-up can give an image but no quantitative information without specialised reconstruction techniques discussed below. Figure adapted from [22].

There are several reasons why eOPT data is not quantitative. The most significant problem is that an unknown number of emitted photons are attenuated within the sample. This requires a mathematical model of attenuation for correction. The second problem is that some incident photons are attenuated before they can cause excitation. This can be compensated for with simultaneous illumination from multiple angles [39]. Another problem identified by Darrell *et al.* is a defocusing effect caused by the lower intensity of of fluorophores positioned outside of the focal plane. Darrell's method of quantifying eOPT data involved a Fourier optics based model which accounted for the defocusing effect and isotropic emission attenuation [40]. A weighting function was calculated based on this model. The function was used in FBP and acts as a window function, spreading the projection information unevenly over the reconstruction image plane.

Kim *et al.* have also published a method for correction of emission attenuation [39]. This method is similar to those used for attenuation correction in SPECT. A co-registered image from tOPT is used to construct an attenuation map and calculate attenuation-survival probabilities for the sample. The probabilities are then used in an iterative OSEM (ordered-subsets expectation-maximisation) reconstruction [39, 41]. This attenuation correction method was tested using a phantom with known fluorescent fibres and corrected images showed more uniform intensity across

the three fibres, differing by 4% in the corrected images but as much as 24% in uncorrected data [39].

In an extension of Kim's method, Thomas *et al.* were the first to report a comprehensive correction for eOPT [42]. Their iterative method corrects for both emission and excitation attenuation and non-uniformities in the light source. Tests of their technique using phantoms show that it can give quantitative information of 3-D fluorophore concentration. This is could be very biologically useful, for example looking at uptake of drugs in tumour treatment.

There have been attempts at performing OPT on live specimen [43–45]. The chief difficulties in this are developing a method limiting scatter and refraction whilst also keeping the specimen alive. Boot and Sharpe reported their efforts for *in vitro* time-lapse quantitative eOPT imaging through tracking GFP expression of a growing mouse embryo limb bud, about 1mm in size [43]. Live OPT has also been used in molecular imaging tracking a changing 3-D gene expression pattern [45]. Vinegoni *et al.* reported *in vivo* imaging of Drosophila melanogaster pupae without clearing or matching fluids [44]. As there is no clearing involved and a mathematical model is required for reconstruction Vinegoni called this 'mesoscopic' imaging rather than OPT/OptCT. Although gathering some biologically interesting information, the resolution was much worse than conventional OPT limiting the applications for this technique. **[Could have great application of monitoring tumour development in 3-D where the mouse could be its own control, since not sacrificing many mice at different stages. Not sure if this is possible due to limited size and resolution, can tumours develop in embryos? Or could we do open imaging with holes in animal?]**

5 Optical Clearing

Optical clearing or clarification is a very important step in OptCT imaging of tissue. Tissue are made up of many components of different refractive indices meaning there are many optical boundaries for scatter and refraction to occur at. This is the reason why visible wavelength light does not penetrate very far in tissue. In order for the parallel ray assumption used in CT reconstruction to be true, refraction and scatter at cell membrane interfaces within the sample must be minimised [38]. This is accomplished with clearing.

During clearing, intracellular fluid is replaced with a optical clearing agent (OCA). There are many choices of OCA but they should all have refractive indices matching the tissue to be imaged and be hyperosmolar (i.e. have a very high solute concentration) [46].

A very popular technique for clearing is the Optical Immersion technique. The sample is set in agarose gel for stability. The gel contains pores which allows diffusion of the OCA. The most commonly used OCAs for OPT are benzyl-alcohol-benzyl-benzoate (BABB, refractive index 1.55) or methyl salicylate (MetSal, refractive index 1.53). These are both aromatic organic solvents and are not miscible in water. Therefore a graded sequence of ethanol and OCA solutions is required to replace the intracellular water with the OCA [38].

Some OCAs, including glycerol and dimethyl sulfoxide (DMSO), can be directly applied to the tissue without need for graded ethanol solutions. However, they have been shown to be less effective than BABB and MetSal and cannot penetrate deeper than 1cm [38]. Glycerol may be more suitable for *in vivo* or live studies as it is biologically inert however DMSO would not be suitable due to high toxicity [47].

Glycerol appears to be the best OCA for clarification of the skin [47,48]. Its refractive index (1.46) is very similar to that of collagen which is the main scatterer in skin. What is unique about glycerol is the clearing effect is reversible upon rehydration with phosphate buffered saline solution [48].

The mechanism for how OCAs bring about optical clarification is not clear. It was previously thought the effect was purely due to refractive index matching however some work has shown that clearing skin with alcohol doesn't correlate with the OCA's refractive index [49, 50]. Additionally glycerol's reversibility indicates that its clarification mechanism is different to other agents. Some proposed mechanisms

include the dissociation of collagen (unravelling of the fibrous structure of collagen) and dehydration (reducing the space between scatterers) as additional clearing effects [47, 51].

Preserving fluorescent signal is very important when clearing for eOPT/OptECT applications. Oldham and Sakhalkar have tested some clearing and fixing protocols with different fluorescent proteins [52, 53]. Although it is common to fix tissue samples with paraformaldehyde (PFA) it was found that this resulted in an almost complete loss of fluorescent signal. Fixation with ethanol was found to preserve fluorescence and keep fluorophores robust upon application of BABB or MetSal. Although BABB was found to give better optical clarity in general, MetSal gave better fluorescence preservation. The optimal procedure was a combination of ethanol fixation and MetSal clearing which was tested on red and green fluorescent proteins (RFP and GFP) [52].

The exact concentrations of OCA needed and the specific OCA used will depend on the tissue and form of imaging to be performed. Finding the optimum chemicals for our purpose will involve trial and error as it has been previously shown that clearing effects are unpredictable due to the complex nature of the interactions between OCA and tissue [47].

6 Optical Staining

6.1 Staining for Cancer Markers

The goal of our investigation will be characterising MRI contrast in tumours by comparison with detailed 3-D maps of histological stains given by OptCT. Staining for tumour recognition and characterisation is a well established area for histology and will be briefly reviewed here. One aspect to be investigated is how these stains work in the presence of OCAs. Unfortunately, Oldham has not found a method of combining immunohistological stains with clearing procedures making *in vivo* staining the most attractive option at present [53].

The primary hallmarks of cancer which are believed to be present in virtually all tumours are listed in Figure 10 [54]. How these acquired capabilities arise differs between individual tumours however, there are some common pathways that can provide targets for therapy. The hallmarks also give some clues for imaging tumours (see Figure 10). Certain genes have been found to be very common in the route to gaining these capabilities. For example, inactivation of the p53 tumour suppressor gene is found in more than 50% of human tumours, giving the tumour cells the ability to evade apoptosis (programmed cell death). This gene can be tracked via reporter genes, such as HSV1-tk(GFP) which can then be imaged with positron emission tomography (PET) [55].

The area of molecular imaging is relatively new and usually involves the use of a reporter gene and complimentary reporter probe, the accumulation of which gives an indication of gene expression [56]. Different reporter probes can be imaged with MRI, PET, SPECT and optical techniques. Optical techniques have the advantage of being more cost and time-effective than MRI or nuclear methods. As mentioned before, OptCT has the additional advantage of better depth penetration than other common optical imaging methods such as confocal microscopy.

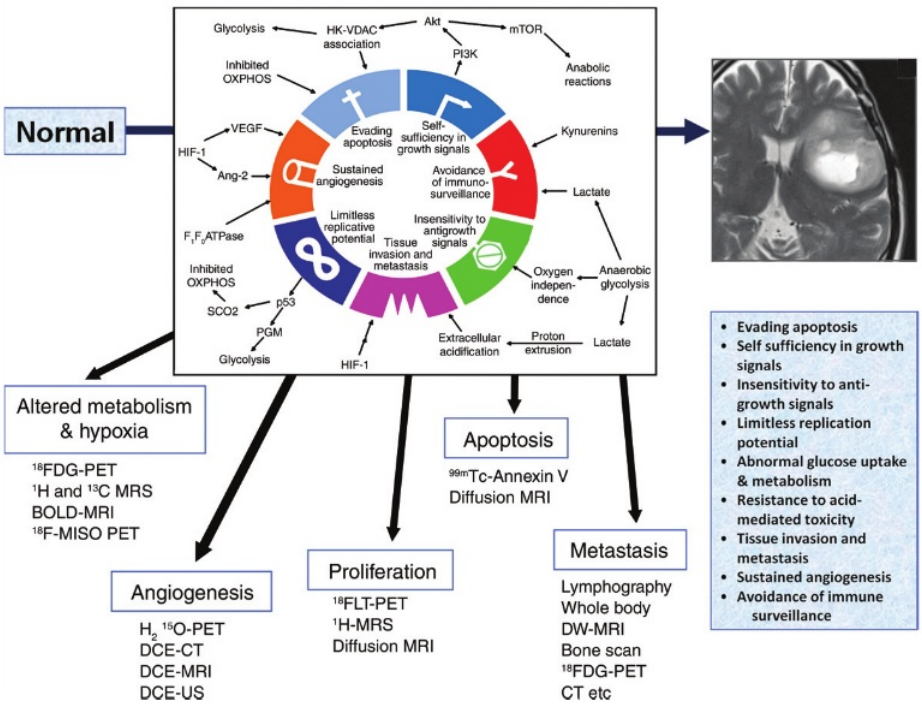

Figure 10: Diagram linking functional imaging modalities to the hallmarks of cancer. *DW*:diffusion weighted, *DCE*:dynamic contrast agent, *Bold*: blood oxygenation-level dependent, *US*: Ultrasound, *MRS*: magnetic resonance spectroscopy, *Ang-2*: angiopoietin-2, *FLT*: fluorothymidine, *HK*: hexokinase, *OXPHOS*: oxidative phosphorylation, *PGM*: phosphoglycerate mutase, *PI3K*: phosphatidylinositol 3-kinase, *SCO2*: synthesis of cytochrome c oxidase 2, *VDAC*: voltage-dependent anion channel. Figure adapted from [1]

.

Fluorescent proteins have revolutionised the area of tumour imaging, allowing real-time imaging of tumour angiogenesis, metastases, cell invasion and motility [57]. Using these proteins can give visualisation of a single metastatic cell in normal tissue, far beyond the ability of histology which is the current gold standard of imaging [58]. The ability to colour-code cells according to genotype and phenotype is a massive advantage when monitoring the progression of tumours and their response to treatment. Some disadvantages of using fluorescent markers include the complication of quantifying the data, high auto-fluorescence in the blue-green window which limits SNR, fluorophore photobleaching and high levels of scatter and attenuation of photons in tissue [59]. However, these problems are being solved as fluorescent imaging

becomes more common-place.

The most common fluorescent marker used is green fluorescent protein (GFP) and its spectrally shifted variants with emission ranges from 442-645nm [57]. The GFP gene was first cloned from *Aequorea victoria* jellyfish and has since been humanised giving high expression and signal for use in mammals [58]. They are popular markers due to their high extinction coefficient and high quantum yield giving very bright and efficient fluorescence. The different variants are spectrally different enough to can be used at the same time, marking different aspects of the biology [57].

With the discovery of red and NIR fluorophores, fluorescent optical molecular imaging is becoming more widespread. These markers avoid the problem of blue-green autofluorescence that GFP experiences and also have slightly deeper penetration due to the therapeutic window in tissue in the NIR range. The first red fluorescent protein (RFP) was cloned from *Discosoma* coral in the late 1990s and has been modified giving DsRed-2, a very bright protein with emission peak at 588nm. Other longer wavelength variants have been developed such as mPlum and mCherry however these were less bright [58]. A newer, very bright red marker called Katushka looks very promising with high photo-stability. Its excitation and emission wavelengths of 588nm and 635nm respectively are ideal for tissue being lowly absorbed by both tissue and haemoglobin [60].

Other fluorescent stains which may be interesting include Doxorubicin, which is a fluorescent drug giving a measure of drug delivery *in vivo* and Evan's blue, a permeability marker which is used clinically. Some non-fluorescent stains which would be used for tOPT include Alcian blue which stains cartilage **(CHECK)**, and Pimonidazole which is a clinically used hypoxia marker giving quantitative and qualitative measures of hypoxia in tissue [61].

Resins such as Mercox and Microphil. HERC (Spelling?), which is a perfusion marker administered *in vivo* **Ask about Herc and resins**

One issue with choosing stains for use in OptCT is finding stains which can diffuse through a whole tumour. Stains administered *in vivo* such as by tail injection may be preferable rather than trying to stain a large volume of tissue after dissection. For example, Soufan *et al.* monitored gene expression during cardiac development in 2003. Their preferred stains could not penetrate the entire embryo heart and they were forced to take slices, losing valuable 3-D information [62].

6.2 Optical Staining in OptCT

One example of fluorescent proteins being used for OptCT imaging is by Kim *et al.* in 2008 [39]. A tumour cell line was genetically labelled with GFP and RFP which were used to image hypoxia-indcible factor 1 (HIF1) and necrotic regions respectively. Tumour micro-vasculature was labelled by a dilute solution of isotonic India ink, a light-absorbing stain administered *in vivo* by tail injection. The use of multiple stains allows co-registered images to be taken using tOPT for the micro-vasculature, eOPT with two different emission filters to see hypoxic regions (GFP) and tumour cells (RFP).

Oldham's group have also used a passive isotonic ink dye to image micro-vasculature but have additionally tested an active Fluorescein isothiocyanate (FITC)-lectin conjugate. The lectin protein binds to the endothelial lining while FITC fluorescence gives eOPT signal [22]. Both agents were administered by tail vein injection before sacrifice of the animal allowing the stains to be circulated by the blood. For imaging tumour cells themselves, HCT116 tumour cells were transfected with a gene coding for RFP and then implanted in the hind leg of a mouse [38]. Using a DSRed2 filter, viable tumour cells were imaged in the OptECT set-up. Oldham demonstrates the superiority of OptCT/ECT for this type of imaging by comparison with μ-CT and μ-MRI (see Figure 11).

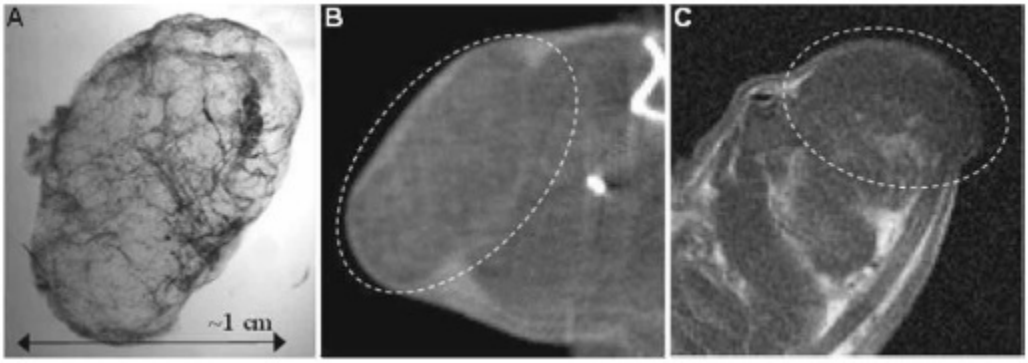

Figure 11: Figure showing the advantage of OptCT imaging over other modalities. Part (A) shows a projection image of a HCT116 tumour after optical clearing. (B) is an *in vivo* μ-CT image of the same tumour with 50μm resolution. (C) is *in vivo* T1 weighted contrast enhanced μ-MRI image of a similar tumour. The superior resolution and contrast in the OptCT image is evident. Images adapted from [38].

.

7 Conclusions

Recent Research Some new ideas include combining with FLIM and FRET.. time gated.. some computational techniques including CLAHE.

Imperial group investigating OPT combined with FRET and FLIM. Define these and some uses for the combined modality. What physical/software changes needed for this imaging. FLIM OPT: [63], In vivo FLIM OPT [64].

Time gated OPT Bassi 2010 [65]

CLAHE Hornblad 2011 [66]

Lorbeer - SLOT [67]

References

[1] A R Padhani and K A Miles. Multiparametric Imaging of Tumor Response to Therapy. *Radiology*, 256(2):348–364, July 2010.

[2] F. Natterer. *The Mathematics of Computerized Tomography*. Classics in Applied Mathematics. Society for Industrial and Applied Mathematics, 2001.

[3] J C Russ. *The Image Processing Handbook*. Image Processing Handbook. Crc Press, 2002.

[4] S J Doran. The history and principles of optical computed tomography for scanning 3-D radiation dosimeters: 2008 update. *Journal of Physics: Conference Series*, 164:012020, June 2009.

[5] Y Wang and R K Wang. Optimization of image-forming optics for transmission optical projection tomography. *Applied optics*, 46(27):6815–6820, 2007.

[6] D Dong, S Zhu, C Qin, V Kumar, J V Stein, S Oehler, C Savakis, J Tian, and J Ripoll. Automated Recovery of the Center of Rotation in Optical Projection Tomography in the Presence of Scattering. 2012.

[7] M J Maryanski, Y Z Zastavker, and J C Gore. Radiation dose distributions in three dimensions from tomographic optical density scanning of polymer gels: Ii. optical properties of the bang polymer gel. *Physics in medicine and biology*, 41(12):2705, 1999.

[8] J C Gore, M Ranade, and M J Maryanski. Radiation dose distributions in three dimensions from tomographic optical density scanning of polymer gels: I. Development of an optical scanner - Abstract - Physics in Medicine and Biology - IOPscience. *Physics in medicine ...*, 1999.

[9] M Oldham, J H Siewerdsen, A Shetty, and D A Jaffray. High resolution gel-dosimetry by optical-CT and MR scanning. *Medical Physics*, 28(7):1436, 2001.

[10] B J Tarte, P A Jardine, and T van Doorn. Laser-scanned agarose gel sections for radiation field mapping. *International Journal of Radiation Oncology* Biology* Physics*, 36(1):175–179, 1996.

[11] R G Kelly, K J Jordan, and J J Battista. Optical CT reconstruction of 3D dose distributions using the ferrous–benzoic–xylenol (FBX) gel dosimeter. *Medical Physics*, 25(9):1741–50, September 1998.

[12] K T S Islam, J F Dempsey, Manisha K Ranade, M J Maryanski, and D A Low. Initial evaluation of commercial optical CT-based 3D gel dosimeter. *Medical Physics*, 30(8):2159, 2003.

[13] Y Xu, C Wuu, and Marek J Maryanski. Determining optimal gel sensitivity in optical CT scanning of gel dosimeters. *Medical Physics*, 30(8):2257, 2003.

[14] Y Xu, C S Wuu, and M J Maryanski. Performance of a commercial optical CT scanner and polymer gel dosimeters for 3-D dose verification. *Medical Physics*, 31(11):3024, 2004.

[15] H S Sakhalkar, J Adamovics, G Ibbott, and M Oldham. A comprehensive evaluation of the PRESAGE/optical-CT 3D dosimetry system. *Medical Physics*, 36(1):71, 2009.

[16] M Oldham. Optical-CT scanning of polymer gels. *Journal of Physics: Conference Series*, 3:122–135, November 2004.

[17] S J Doran, K K Koerkamp, M A Bero, P Jenneson, E J Morton, and W B Gilboy. A CCD-based optical CT scanner for high-resolution 3D imaging of radiation dose distributions: equipment specifications, optical simulations and preliminary results. *Physics in Medicine and Biology*, 46(12):3191–3213, November 2001.

[18] N Krstajić and S J Doran. Focusing optics of a parallel beam CCD optical tomography apparatus for 3D radiation gel dosimetry. *Physics in Medicine and Biology*, 51(8):2055–2075, April 2006.

[19] B J Tarte, P A Jardine, T van Doorn, K N Nitschke, and M G Poulsen. Development of a CCD array imaging system for measurement of dose distributions in doped agarose gels. *Medical Physics*, 24:1521, 1997.

[20] J R Walls, J G Sled, J Sharpe, and R M Henkelman. Correction of artefacts in optical projection tomography. *Physics in Medicine and Biology*, 50(19):4645–4665, September 2005.

[21] H S Sakhalkar and M Oldham. Fast, high-resolution 3D dosimetry utilizing a novel optical-CT scanner incorporating tertiary telecentric collimation. *Medical Physics*, 35(1):101, 2008.

[22] M Oldham, H Sakhalkar, Y M Wang, P Guo, T Oliver, R Bentley, Z Vujaskovic, and M Dewhirst. Three-dimensional imaging of whole rodent organs

using optical computed and emission tomography. *Journal of Biomedical Optics*, 12(1):014009, 2007.

[23] N Krstajić and S J Doran. Fast laser scanning optical-CT apparatus for 3D radiation dosimetry. *Physics in Medicine and Biology*, 52(11):N257–N263, May 2007.

[24] J G Wolodzko, C Marsden, and A Appleby. CCD imaging for optical tomography of gel radiation dosimeters. *Medical Physics*, 26:2508, 1999.

[25] J Hsieh. *Computed Tomography: Principles, Design, Artifacts, and Recent Advances*. SPIE Press monograph. SPIE Press, 2003.

[26] T Olding and L J Schreiner. Cone-beam optical computed tomography for gel dosimetry II: imaging protocols. *Physics in Medicine and Biology*, 56(5):1259–1279, February 2011.

[27] A Thomas, J Newton, and M Oldham. A method to correct for stray light in telecentric optical-CT imaging of radiochromic dosimeters. *Physics in Medicine and Biology*, 56(14):4433–4451, June 2011.

[28] J Sharpe. Optical Projection Tomography as a Tool for 3D Microscopy and Gene Expression Studies. *Science*, 296(5567):541–545, April 2002.

[29] R H Webb. Confocal optical microscopy. *Reports on Progress in Physics*, 59:427–471, 1996.

[30] D Huang, E A Swanson, C P Lin, J S Schuman, W G Stinson, W Chang, M R Hee, T Flotte, K Gregory, C A Puliafito, et al. *Optical coherence tomography*. PhD thesis, Massachusetts Institute of Technology, Whitaker College of Health Sciences and Technology, 1993.

[31] J Sharpe. Optical projection tomography as a new tool for studying embryo anatomy. *Journal of Anatomy*, 202(2):175–181, February 2003.

[32] V V Tuchin, X Xu, and R K Wang. Dynamic Optical Coherence Tomography in Studies of Optical Clearing, Sedimentation, and Aggregation of Immersed Blood. *Applied optics*, 41(1):258–271, 2002.

[33] W. Xia, R.M. Lewitt, and P.R. Edholm. Fourier correction for spatially variant collimator blurring in spect. *Medical Imaging, IEEE Transactions on*, 14(1):100–115, 1995.

[34] J R Walls, J G Sled, J Sharpe, and R M Henkelman. Resolution improvement in emission optical projection tomography. *Physics in Medicine and Biology*, 52(10):2775–2790, April 2007.

[35] M Fauver, E J Seibel, J R Rahn, M G Meyer, F W Patten, T Neumann, and A C Nelson. Three-dimensional imaging of single isolated cell nuclei using optical projection tomography. *Opt. Express*, 13(11):4210–4223, 2005.

[36] G Häusler. A method to increase the depth of focus by two step image processing. *Optics Communications*, 6(1):38–42, 1972.

[37] Y Wang and R Wang. Imaging using parallel integrals in optical projection tomography. *Physics in Medicine and Biology*, 51(23):6023–6032, October 2006.

[38] M Oldham, H Sakhalkar, T Oliver, Y M Wang, J Kirkpatrick, Y Cao, C Badea, G A Johnson, and M Dewhirst. Three-dimensional imaging of xenograft tumors using optical computed and emission tomography. *Medical Physics*, 33(9):3193, 2006.

[39] E Kim, J Bowsher, A S Thomas, H Sakhalkar, M Dewhirst, and M Oldham. Improving the quantitative accuracy of optical-emission computed tomography by incorporating an attenuation correction: application to HIF1 imaging. *Physics in Medicine and Biology*, 53(19):5371–5383, September 2008.

[40] A Darrell, H Meyer, K Marias, M Brady, and J Ripoll. Weighted filtered backprojection for quantitative fluorescence optical projection tomography. *Physics in Medicine and Biology*, 53(14):3863–3881, June 2008.

[41] H.M. Hudson and R.S. Larkin. Accelerated image reconstruction using ordered subsets of projection data. *Medical Imaging, IEEE Transactions on*, 13(4):601–609, 1994.

[42] A Thomas, J Bowsher, J Roper, T Oliver, M Dewhirst, and M Oldham. A comprehensive method for optical-emission computed tomography. *Physics in Medicine and Biology*, 55(14):3947–3957, June 2010.

[43] M J Boot, C H Westerberg, J Sanz-Ezquerro, J Cotterell, R Schweitzer, M Torres, and J Sharpe. In vitro whole-organ imaging: 4D quantification of growing mouse limb buds. *Nature Methods*, 5(7):609–612, May 2008.

[44] C Vinegoni, C Pitsouli, D Razansky, N Perrimon, and V Ntziachristos. In vivo imaging of Drosophila melanogaster pupae with mesoscopic fluorescence tomography. *Nature Methods*, 5(1):45–47, December 2008.

[45] J F Colas and J Sharpe. Live optical projection tomography. *Organogenesis*, 5(4):211–216, 2009.

[46] V V Tuchin and Society Of Photo-Optical Instrumentation Engineers. *Tissue Optics: Light Scattering Methods and Instruments for Medical Diagnosis*. Press Monographs. SPIE/International Society for Optical Engineering, 2007.

[47] X Wen, V V Tuchin, Q Luo, and D Zhu. Controling the scattering of Intralipid by using optical clearing agents. *Physics in Medicine and Biology*, 54(22):6917–6930, November 2009.

[48] G Vargas, E K Chan, J K Barton, H G Rylander, and A J Welch. Use of an Agent to Reduce Scattering. *Lasers in Surgery and Medicine*, 24(2):133–41, 1999.

[49] B Choi, L Tsu, E Chen, T S Ishak, S M Iskandar, S Chess, and J S Nelson. Determination of chemical agent optical clearing potential using in vitro human skin. *Lasers in Surgery and Medicine*, 36(2):72–75, 2005.

[50] Z Mao, D Zhu, Y Hu, X Wen, and Z Han. Influence of alcohols on the optical clearing effect of skin in vitro. *Journal of Biomedical Optics*, 13(2):021104–021104, 2008.

[51] A T Yeh, B Choi, J S Nelson, and B J Tromberg. Reversible Dissociation of Collagen in Tissues. *The Journal of Investigative Dermatology*, 121(6):1332–5, 2003.

[52] H S Sakhalkar, M Dewhirst, T Oliver, Y Cao, and M Oldham. Functional imaging in bulk tissue specimens using optical emission tomography: fluorescence preservation during optical clearing. *Physics in Medicine and Biology*, 52(8):2035–2054, March 2007.

[53] M Oldham, H Sakhalkar, T Oliver, G Allan Johnson, and M Dewhirst. Optical clearing of unsectioned specimens for three-dimensional imaging via optical transmission and emission tomography. *Journal of Biomedical Optics*, 13(2):021113, 2008.

[54] D Hanahan and R A Weinberg. The hallmarks of cancer. *Cell*, 100(1):57–70, 2000.

[55] M Doubrovin, V Ponomarev, T Beresten, J Balatoni, W Bornmann, R Finn, J Humm, S Larson, M Sadelain, R Blasberg, and et al. Imaging transcriptional regulation of p53-dependent genes with positron emission tomography in vivo. *Proceedings of the National Academy of Sciences of the United States of America*, 98(16):93005, 2001.

[56] R Blasberg. Molecular imaging and cancer. *Molecular cancer therapeutics*, 2(3):335–43, 2003.

[57] R Hoffman. The multiple uses of fluorescent proteins to visualize cancer in vivo. *Nature reviews. Cancer*, 5(10):796–806, 2005.

[58] R M Hoffman. Imaging cancer dynamics in vivo at the tumor and cellular level with fluorescent proteins. *Clinical and Experimental Metastasis*, 26:345–355, 2009.

[59] S Gross and D Piwnica-Worms. Spying on cancer: molecular imaging in vivo with genetically encoded reporters. *Cancer cell*, 7(1):5–15, 2005.

[60] D Shcherbo, E Merzlyak, T Chepurnykh, A Fradkov, G Ermakova, El Solovieva, K Lukyanov, E Bogdanova, A Zaraisky, S Lukyanov, and et al. Bright far-red fluorescent protein for whole-body imaging. *Nature methods*, 4(9):741–6, 2007.

[61] M Varia, D Calkins-Adams, L Rinker, A Kennedy, D Novotny, W Fowler, and J Raleigh. Pimonidazole: a novel hypoxia marker for complementary study of tumor hypoxia and cell proliferation in cervical carcinoma. *Gynecologic oncology*, 71(2):270–277, 1998.

[62] A T Soufan, J M Ruijter, M J B van den Hoff, P A J de Boer, J Hagoort, and A F M Moorman. Three-dimensional reconstruction of gene expression patterns during cardiac development. *Physiological genomics*, 13(3):187–195, 2003.

[63] J McGinty, K B Tahir, R Laine, C B Talbot, C Dunsby, M A A Neil, L Quintana, J Swoger, J Sharpe, and P M W French. Fluorescence lifetime optical projection tomography. *Journal of Biophotonics*, 1(5):390–394, October 2008.

[64] J McGinty, H B Taylor, L Chen, L Bugeon, J R Lamb, M J Dallman, and P M W French. In vivo fluorescence lifetime optical projection tomography. *Biomedical optics express*, 2(5):1340–1350, 2011.

[65] A Bassi, D Brida, C D'Andrea, G Valentini, R Cubeddu, S De Silvestri, and G Cerullo. Time-gated optical projection tomography. *Optics letters*, 35(16):2732–2734, 2010.

[66] A Hörnblad, A Cheddad, and U Ahlgren. An improved protocol for optical projection tomography imaging reveals lobular heterogeneities in pancreatic islet and -cell mass distribution. *Islets*, 3(4):204–208, July 2011.

[67] R A Lorbeer, M Heidrich, C Lorbeer, D F Ramírez Ojeda, G Bicker, H Meyer, and A Heisterkamp. Highly efficient 3D fluorescence microscopy with a scanning laser optical tomograph. *Optics Express*, 19(6):5419–5430, 2011.